

Robust real-time imaging through flexible multimode fibers

Abdullah Abdulaziz^{1*}, Simon Peter Mekhail², Yoann Altmann¹, Miles J. Padgett² and Stephen McLaughlin¹

^{1*}School of Engineering and Physical Sciences, Heriot-Watt University, Edinburgh, United Kingdom.

²School of Physics and Astronomy, University of Glasgow, Glasgow, United Kingdom.

*Corresponding author(s). E-mail(s): A.Abdulaziz@hw.ac.uk;

Contributing authors: Simon.Mekhail@glasgow.ac.uk;

Y.Altmann@hw.ac.uk; Miles.Padgett@glasgow.ac.uk;

S.McLaughlin@hw.ac.uk;

Abstract

Conventional endoscopes comprise a bundle of optical fibers, associating one fiber for each pixel in the image. In principle, this can be reduced to a single multimode optical fiber (MMF), the width of a human hair, with one fiber spatial-mode per image pixel. However, images transmitted through a MMF emerge as unrecognisable speckle patterns due to dispersion and coupling between the spatial modes of the fiber. Furthermore, speckle patterns change as the fiber undergoes bending, making the use of MMFs in flexible imaging applications even more complicated. In this paper, we propose a real-time imaging system using flexible MMFs, but which is robust to bending. Our approach does not require access or feedback signal from the distal end of the fiber during imaging. We leverage a variational autoencoder (VAE) to reconstruct and classify images from the speckles and show that these images can still be recovered when the bend configuration of the fiber is changed to one that was not part of the training set. We utilize a MMF 300 mm long with a 50 μm core for imaging 10×10 cm objects placed approximately at 20 cm from the fiber and the system can deal with a change in fiber bend of 50° and range of movement of 8 cm.

Keywords: Bending multimode fiber, Gaussian mixture variational autoencoder, endoscopy, image reconstruction

1 Introduction

Multimode fibers (MMFs), the width of a human hair, potentially allow for the transmission of images formed from the thousands of spatial modes they support [1, 2]. This creates the potential for minimally-invasive and high-resolution imaging systems such as ultra-thin endoscopes which can be used for imaging objects out of the reach of conventional technology. Unfortunately, even when using temporally coherent light, images propagated through MMFs suffer from severe spatial distortions and can appear as random speckle patterns at the distal end due to modal dispersion in the fiber [1, 2]. However, although the information is completely scrambled at either end of a MMF, the vast majority of the information is not lost and hence the image can, in principle, be recovered.

To image through MMFs, two main classes of methods have been used to date. The first consists of raster-scanning methods [2–8], which rely on measuring the complex mapping of the input field onto the output field, namely the transmission matrix (TM) [9–13]. Using the TM, the input field at the proximal facet of a MMF can be specified such that focused light beams are generated at the distal end. By calculating the correct series of input fields, this focused beam can be scanned over an object with a field of view defined by the numerical aperture of the fiber. The second class of methods consists of speckle imaging approaches [14–17]. With these methods, a set of speckle patterns is recorded at the distal end of a MMF, forming a measurement matrix during a calibration stage. During imaging, the same speckle patterns are projected sequentially onto a new object and the collected overall signal provides a speckle measurement. Iterative methods have been traditionally used to reconstruct objects from the speckle measurements and the measurement matrix. Although Lan *et al.* in [17] has shown that using an average of speckle patterns recorded for different fiber bends during image reconstruction can decrease the influence of changing the fiber bend, all the aforementioned methods are not robust to bending and consider a single, static, fiber configuration. It should be noted at this stage that although in principle the light propagation in MMFs is often invertible, raster scanning leads to better results due to better signal-to-noise (SNR) ratios.

To overcome the fiber bending problem and allow the use of MMFs as flexible imaging devices, extensive research has been carried out over the last decade. The authors in [18] proposed a real-time TM measurement technique that allows for light refocusing at very high frame rates by placing a photodetector at the distal end of the fiber. In another example, Farahi *et al.* in [19] placed a virtual coherent point light source (a beacon) at the distal end to allow for bending compensation while focusing light through MMFs by digital

phase conjugation (DPC). Similarly, Gu *et al.* in [20] attached a partial reflector to the distal end of the MMF, which reflects light back to the proximal end, allowing the MMF to be re-calibrated each time the fiber is bent. Leveraging optical memory effects, the authors of [21] claimed that the use of a guide-star on the distal facet of a MMF, which reports its local field intensity to the proximal facet, and the estimate of a basis in which the TM is diagonal, enables an approximation of TM and thus allowed imaging through a bending MMF. All these methods require a prior computation of the TM or feedback mechanism from the distal end of the fiber. Plöschner *et al.* in [6] showed that bending deformations in step-index MMFs could be predicted and compensated for for imaging applications. However, this process is computationally intensive and requires precise knowledge of the fiber layout.

Recently, deep learning approaches [22–32] have emerged that infer images from speckle patterns without prior knowledge of the fiber characteristics. Although they demonstrate promising results and real-time reconstruction, accounting for fiber bending remains a challenging problem. In this context, Li *et al.* in [33, 34] showed that training an autoencoder (AE) neural network on speckles from multiple thin diffusers can be used to recover images from speckles corresponding to a new diffuser of the same type. Moreover, the authors in [35] confirmed the existence of statistical dependencies in the optical field distribution scattered by a random medium. Motivated by these finding, Resisi *et al.* in [36] extended the work of Li *et al.* [33, 34] to MMFs and showed that an AE trained on hundreds of fiber bends can be used to reconstruct images from new configurations. However, their results were limited to the reconstruction of handwritten digits, which share very similar features, displayed on a binary DMD. Furthermore, the reflected light from the fiber was imaged on a camera which does not depict a realistic imaging scenario. Finally, preparing the data for training and testing required 14 weeks of lab work.

In this paper, we propose a high-resolution and minimally-invasive imaging system leveraging MMFs. In contrast to previously reported work, our proposed framework represents a more realistic imaging scenario where no access to the distal end of the fiber is required during imaging and the collected signal need not be coherent light. We use speckle patterns to probe an object through an illumination MMF while a secondary collection fibre, placed alongside the illumination fibre, transmits the diffuse reflections from a Lambertian-like object back to the proximal end to be recorded by an avalanche photodiode (APD). To recover the object from APD measurements, we leverage a variational autoencoder with a Gaussian mixture latent space (GMVAE). In contrast to black-box AEs, the problem is posed in a Bayesian framework and the posterior distribution representing the complicated mapping between measurements corresponding to different fiber configurations and the underlying images of different classes is learnt in a low-dimensional latent representation. The latent space learned is configuration-agnostic. This means all measurement vectors corresponding to the same class of images but to different fiber configurations share the same cluster in the latent space. The architecture of

GMVAE is much simpler than that of the AE proposed in [33, 34] and as a result the training time is reduced by around 90% for the same training data set. Our light network is smaller than [33, 34] but does not suffer as much from generalization issues as the architecture reported in [36]. We demonstrate the robustness of our GMVAE against AE [33, 34] on new image classes from the fashion-MNIST data set and new configurations of a MMF that were not used during training. This work paves the way for flexible, inexpensive and high-resolution imaging system for use in cases which are highly sensitive to implant size.

2 Optical setup

The experimental setup, shown in Fig. 1, consists of a Q-switched laser at 532 nm with a pulse width of 700 ps and a repetition rate of 21 kHz (Teem Photonics SNG-100P-1x0). The laser is spatially shaped by a digital micro-mirror device (Vialux V-7000) (DMD) such that the far-field of the distal end of a 62.5 μm core graded index fiber with a numerical aperture (NA) of 0.275 (Thorlabs GIF625) has a desired spatial intensity pattern. Through calibration of the fiber in a particular configuration, this spatial pattern was selected to be a raster scanning spot as is described in section 5.1. As will be discussed in section 5.2, we also investigated the case where the holograms are not selected for any specific configuration of fiber and, hence, the DMD masks were generated with a quasi-random algorithm. For imaging, a sample image is placed at the screen and the reflected light for each of M patterns generated by the DMD is collected by a second step index collection fiber,

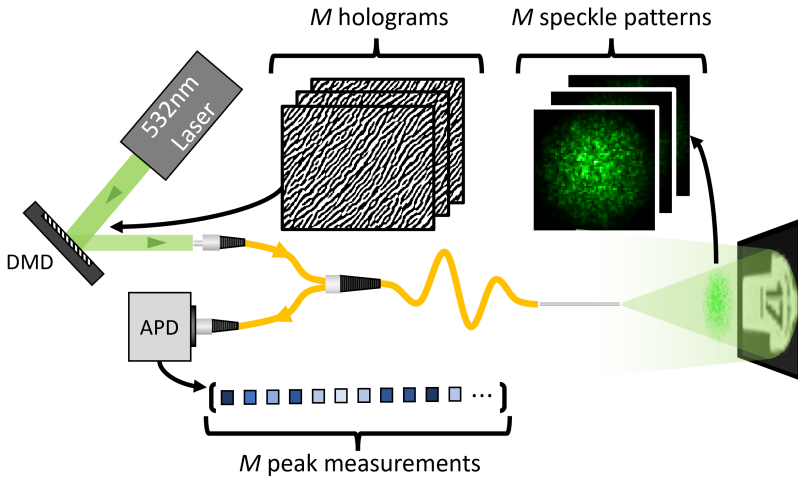


Fig. 1: Simplified experimental setup for reflective imaging through an optical fiber. Illumination and collection fibers are signified by propagation arrows. DMD - digital micro-mirror device, APD - avalanche photodiode.

400 μm core and 0.39 NA (Thorlabs FT400UMT), running parallel to the illumination fiber. The back-scattered light is recorded at the proximal end of the collection fiber by an AC-coupled avalanche photodiode (MenloSystems APD210) (APD) sampling at 2.5 Gs/s. The laser pulses are used a trigger for imaging and as such allow for time gating the signal from the collection fiber. In this way only data corresponding to the distance of the sample from the fiber tip are considered and the remaining recording could be dismissed, hence reducing background illumination effects. After this temporal gating is performed, M speckle measurements remain for each image. This imaging system does not require access to- or a feedback signal from the distal end of the fiber during imaging.

Assuming that the speckle patterns projected at the distal end of the fiber are known (we will discuss in section 4 how they are recorded before actual imaging), each measurement received by the APD can be modeled as the overlap integral between the object and one speckle pattern, hence the forward model can be formulated as

$$\mathbf{y} = \mathcal{G}(\mathbf{A}\mathbf{x}) + \mathbf{n}, \quad (1)$$

where $\mathbf{y} \in \mathbb{R}^M$ is the measurement vector, $\mathbf{A} \in \mathbb{R}^{M \times N}$ is the measurement matrix which contains the set of M speckle patterns, vectorized to form the rows of the matrix, each of size N pixels. The vector $\mathbf{x} \in \mathbb{R}^N$ is a discretized version of the object to be reconstructed and $\mathbf{n} \in \mathbb{R}^M$ represents measurement noise, modelled as a realization of a random i.i.d. Gaussian noise. The function \mathcal{G} comprises the damping effect caused by the collection fiber and the perturbations of the APD and the laser (see suppl. materials for details). As discussed in the introduction, estimating the underlying object \mathbf{x} from the measurements \mathbf{y} yields an inverse problem that can be solved efficiently using a variety of different methods, provided that \mathbf{A} and $\mathcal{G}(\cdot)$ do not change. However, as illustrated in Figure 3, changing the configuration of the fiber means significant changes in the measurement matrix \mathbf{A} , and hence the measurement values. Thus, system re-calibration is usually performed to correct for changes in the measurement matrix \mathbf{A} . In this work, we aim to learn an \mathbf{A} -agnostic variational autoencoder that can generalize, to some extent, to new and unseen configurations of the fiber.

3 Reconstruction algorithm

Variational autoencoders (VAEs) [37, 38] are deep generative models that consist of an encoder, a latent space and a decoder. The essence of VAEs is to regularize the encodings distribution during training to ensure that the latent space captures only the important features of the data set. This allows for reconstruction (or generation) of new data through the decoder. In contrast to the standard VAE architecture which only contains a single continuous (and multivariate) latent variable, the Gaussian mixture VAE (GMVAE) [39–43]

also contains a discrete latent variable representing the data class. Therefore, by specifying different integer numbers to different object classes, the GMVAE provides the membership probabilities of the observed object, for all the pre-defined classes, which allows for object classification.

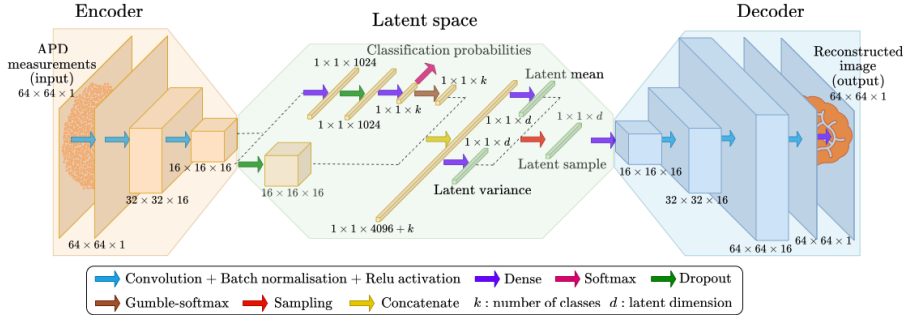


Fig. 2: Schematic of the proposed Gaussian mixture variational autoencoder.

In this context, we leverage a GMVAE (depicted in Fig. 2) for imaging through a MMF which bends. Essentially, the encoder of our GMVAE performs non-linear dimensionality reduction of a set of APD measurements corresponding to any image and any fiber configuration into a low-dimensional latent representation which only captures image information and disregards the fiber configuration. Thus, the learnt latent space is trained to be \mathbf{A} -agnostic, i.e. all measurement vectors corresponding to the same image but different fiber configurations share the same features in the latent space. The decoder of the GMVAE then takes as input this latent vector and generates an estimated image of the scene. Once trained, the proposed GMVAE is able to simultaneously classify (through the VAE encoder) and reconstruct (through the VAE decoder) objects from measurement vectors corresponding to a variety of fiber configurations, even configurations unseen during training.

4 Training procedure

Recall that training the GMVAE above requires sets of input (APD measurements) and output (reference images of objects, belonging to different classes). However, recording sufficient measurement vectors at different fiber configurations and with a large image data base for training is not possible in practice as this imaging system is based on a sequential generation of illumination patterns in order to record diffuse reflection from real objects. To circumvent this problem, we use a white screen and a scientific CMOS camera (Hamamatsu Orca Flash 4.2) (sCMOS) to record the speckle patterns corresponding to M fixed DMD patterns for different configurations of the fiber. This leads to different speckle matrices \mathbf{A}_l , where each speckle is a row vector in \mathbf{A}_l

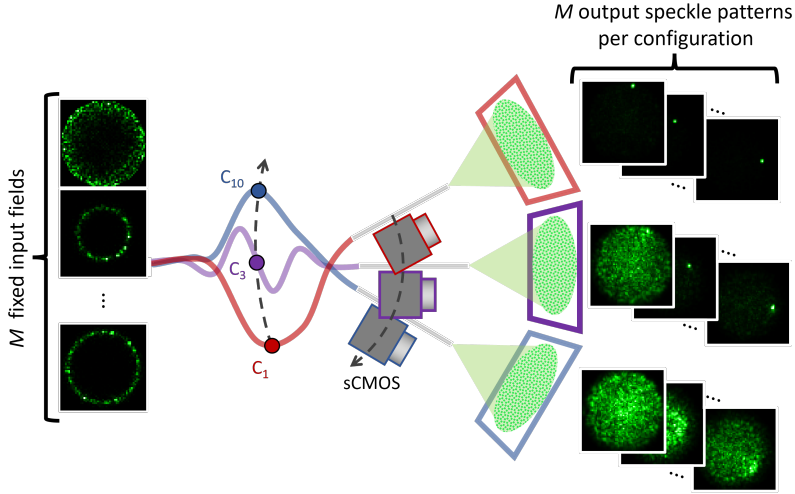


Fig. 3: Optical setup for collecting the training data set showing three simplified fiber configuration examples and the resulting changes to the output speckle patterns. The fiber tip, imaging screen, and sCMOS camera were rotated together using the rotation stage and the middle of the fiber was clamped to- and moved by the bending arm.

and l represents the index of the fiber configuration, as illustrated in Fig. 3. The DMD patterns, and therefore input spatial light field, are maintained for all configurations which allows the model to capture the hidden correlations between speckle patterns corresponding to the different configurations. We then use the recorded \mathbf{A}_l matrices to perform speckle projection on images numerically to simulate measurement vectors. More precisely, we compute \mathbf{y} as in Equation (1) for each image \mathbf{x} in our training dataset and for all the l configurations of the fiber (replacing \mathbf{A} in Equation (1) by \mathbf{A}_l).

To assess quantitatively the performance of the model in the next section, we first generate data sets in a similar fashion to the training data, however, we record speckle patterns corresponding to new configurations of the fiber which are different from those seen during training. We then perform projection on the test images numerically to simulate measurements. Measurements computed with this procedure are referred to as numerical measurements. We also assess qualitatively the performance of GMVAE on real measurements collected by an APD as presented in Fig. 1. We refer to these measurements as APD measurements. Training using numerical measurements offers the benefit of greater speed and flexibility to the model as learning new classes of images does not require the lab experiments to be repeated.

5 Experiments

In the following experiments, we apply two types of bend simultaneously on the fiber. These are rotational bends applied at the final section of the fiber using a rotational stage, and arm bends performed on the middle section of the fiber leveraging a large lever arm (the experimental setup is shown in suppl. materials). The lever arm has a mechanical advantage of $\sim 1:8$ from the actuation side to the fiber-clamp side. Arm bends were measured at the actuation side in -1 mm increments from the initial position at 10 mm to 0 mm while rotational bends were in 5° increments from the initial position at 230° to 280° . This yielded $L = 11$ different fiber configurations starting from (10 mm, 230°) to the final position (0 mm, 280°). For simplicity, we denote each configuration by C_x where x is the corresponding arm bend position.

GMVAE training was performed using $L = 5$ fiber configurations (C_{10} , C_7 , C_5 , C_3 and C_1). These configurations cover the range from (10 mm, 230°) to (1 mm, 275°). At each configuration, we use 6000 images from each of the following 8 classes of the fashion-MNIST data set: (0) t-shirt, (1) trouser, (2) dress, (3) coat, (4) sandal, (5) shirt, (6) sneaker, and (7) boot. Testing was done on new configurations (C_9 , C_8 , C_6 , C_4 , C_2 , C_0) using new images from the same trained-on 8 classes and 2 new classes: pullover and bag. Here, C_9 , C_8 , C_6 , C_4 , C_2 represent new bends which lie inside the range of the training configurations while C_0 (0 mm, 280°) represents a new bend which lies outside the range of the training configurations.

We tested the method in two scenarios, with and without wavefront shaping. Note that wavefront shaping allows for raster-scanning imaging while no wavefront shaping leads to speckle imaging. The performance of GMVAE is evaluated in terms of reconstruction quality against AE [33, 34] on numerical and APD measurements. Note that numerical measurements are computed at all $L = 11$ configurations while the APD measurements are only recorded at C_{10} , C_7 , C_5 , C_2 and C_0 . Since AE can only perform reconstruction, the classification accuracy of GMVAE is compared to that of a classifier trained on the images reconstructed by AE. For fairness, the chosen classifier, denoted by C-AE, has the same architecture as that used in our GMVAE (see suppl. materials for details).

5.1 First experiment with wavefront shaping

In this experiment, we use the wavefront shaping technique as in [2] to generate focal spots at the distal end of the fiber. This allows for raster-scanning imaging which can give better results due to better SNR ratios. Speckles were recorded at the different configurations and wavefront shaping was only performed at the configuration C_{10} . This means that speckles at C_{10} (10 mm, 230°) are simple focal points (see Fig. 4, (a)). By bending the fiber away from the calibration position, the focal points become speckles due to coupling between spatial modes of the fiber. Therefore, C_0 (0 mm, 280°) represents the most challenging bend where speckles have the maximum distortion (see Fig. 4, (c)).

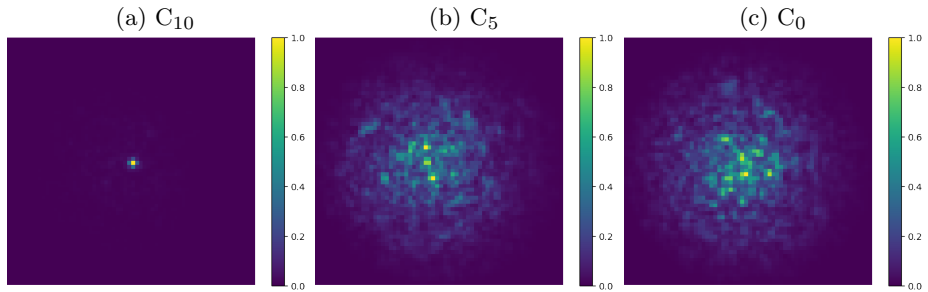


Fig. 4: First experiment with wavefront shaping: speckles from a fixed DMD phase mask recorded at different fiber configurations: (a) C_{10} , (b) C_5 and (c) C_0 .

Fig. 5, (a) shows the peak signal-to-noise ratio (PSNR) curves obtained by GMVAE and AE at all configurations under scrutiny utilizing 10000 numerical measurements and 20 APD measurements from the fashion-MNIST dataset (8 trained-on classes and 2 new classes). We notice that both GMVAE and AE give the best reconstruction quality on the numerical measurements recorded at C_{10} (AE scores $\text{PSNR} = 23.67 \pm 3.79$ dB and GMVAE scores $\text{PSNR} = 22.69 \pm 3.61$ dB). This is expected since C_{10} was used during training. Moreover, C_{10} is the calibrated configuration, hence details from the original images can be seen directly in the measurements, reducing the problem of reconstruction to a denoising or a mild deconvolution problem. Although, AE was able to achieve 1 dB enhancement on numerical measurements at the calibrated configuration, GMVAE achieves higher PSNR values at all other configurations. In contrast to the AE which exhibits a gradual decrease in PSNR values on numerical measurements as the fiber bends away from the calibrated position, GMVAE maintains almost the same PSNR values (≈ 20 dB) at the seen configurations (C_7 , C_5 , C_3 and C_1) and the same PSNR values (≈ 18.5 dB) at the unseen configurations (C_9 , C_8 , C_6 and C_4 , C_2 and C_0). Albeit not significant, the difference in PSNR values between seen and unseen configurations suggests that not all the configuration-dependant features are discarded in the latent space, hence training the GMVAE with more configurations might lead to better generalization. GMVAE also maintains around 1.5 dB of PSNR enhancement on APD measurements recorded at the seen configurations (C_{10} , C_7 and C_5) and the unseen configurations (C_2 and C_0). Since both the AE and GMVAE were trained on numerical measurements, we notice a steep decrease in the PSNR values when testing on APD measurements. Although the training procedure was adapted to partially compensate for the damping effect caused by the collection fiber and the perturbations of the APD and the laser (see suppl. materials for details), small additional variations occur in the ADP measurement. On the one side, this suggests the use of a more robust hardware and possibly enhance the forward model to improve the training efficiency. On the other hand, this demonstrates the performance of the methods in realistic scenarios including unknown signal variations.

Fig. 6 compares qualitatively the reconstruction quality of GMVAE against AE on APD measurements collected at the following configurations: C_{10} , C_2 and C_0 . We can clearly see the good reconstruction quality for both GMVAE and AE at the calibrated configuration C_{10} . Again, the results show a superior performance for the GMVAE in comparison to AE for the new configurations (C_2 and C_0) which are far away from the calibration position. Although C_0 represents the most difficult bend which lies outside the range of training configurations, the GMVAE was able to maintain almost the same reconstruction quality as that for C_2 which lies inside the training range. This shows the ability of the GMVAE to generalize to new configurations of the fiber in comparison with AE that fails in capturing the non-linear dependencies between the different configurations. Moreover, the computational time of GMVAE is around 10 times lower than that for AE.

Fig. 7 shows the average confusion matrices obtained by the GMVAE and C-AE on 8000 numerical measurements from the 8 trained-on classes. The confusion matrices are averaged over the unseen configurations C_9 , C_8 , C_6 , C_4 , C_2 and C_0 . We can see that the GMVAE achieves $77 \pm 3\%$ classification accuracy with 1% average enhancement over C-AE which scores $76 \pm 8\%$. These numbers suggest that simultaneous learning is better than sequential learning and can boost both reconstruction quality and classification accuracy for unseen configurations of the fiber.

Fig. 8 presents the combined raw data and the combined GMVAE latent vectors of 8000 numerical measurements computed at the configurations C_{10} , C_2 and C_0 and projected using principal component analysis (PCA) to the 3D space. In contrast to the combined raw data (Fig. 8, (a)), the GMVAE combined latent space (Fig. 8, (b)) of the testing data points shows a clear separation between the different classes. More importantly, the combined latent space is configuration-agnostic. This means all measurement vectors corresponding to the same class but different fiber configurations share the same cluster in the latent space.

5.2 Second experiment without wavefront shaping

In the second experiment, speckles were recorded at the different configurations with no configuration-specific wavefront shaping performed. This simulates a situation in which no prior calibration has been done and the fiber is to be used in-situ for imaging directly. This experiment represents a more complicated scenario as all configurations are challenging (see Fig. 9). However, it could be of interest when wavefront shaping for raster scanning is expensive or not possible.

Fig. 5, (b) presents the PSNR curves obtained by GMVAE and AE at all configurations on numerical and APD measurements. We see that the GMVAE achieves higher PSNR values (around 2 dB) for all configurations on both numerical and APD measurements. The GMVAE gives almost the same PSNR values at the seen configurations and the same PSNR values at the unseen

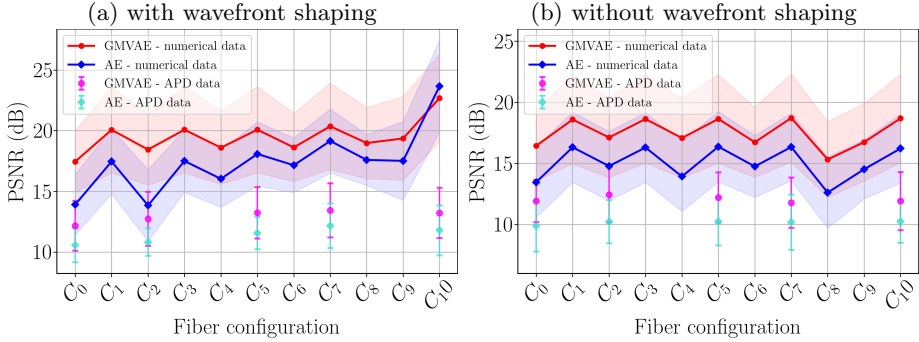


Fig. 5: Average PSNR curves obtained by GMVAE and AE at different configurations on 10000 numerical measurements and 20 APD measurements from the fashion-MNIST dataset (8 trained-on classes and 2 new classes). (a) results of the first experiment with wavefront shaping and (b) results of the second experiment without wavefront shaping.

configurations (except for C₈). The drop in PSNR values at the unseen configurations indicates that the GMVAE latent space does not only capture image information but also fiber configuration related information. This problem might be mitigated by increasing the number of training configurations.

The average confusion matrices obtained by GMVAE and C-AE on 8000 numerical measurements from the 8 trained-on classes are shown in Fig. 10. The confusion matrices are averaged over the unseen configurations. Once again, the results suggest better classification accuracy for the GMVAE compared to C-AE. More precisely, GMVAE scores $66 \pm 10\%$ with 8% average enhancement from C-AE.

Finally, the combined raw data and the combined GMVAE latent vectors of 8000 numerical measurements computed at the configurations C₅, C₂ and C₀ and projected by PCA to the 3D space are presented in Fig. 11. In contrast to the combined raw data (Fig. 8, (a)) where we can see stripes representing measurements from the same class but different configurations, the combined GMVAE latent space (Fig. 8, (b)) is configuration-agnostic, i.e. only features of the measurements related to the underlying images are preserved and configuration-dependent features are discarded.

5.3 Video reconstruction

We further validate the performance of the GMVAE on recorded videos in two scenarios. Firstly, we show the reconstruction of 3 static objects while moving the fiber from C₁₀ (the calibrated position) to C₅. Secondly, we show the reconstruction of a moving object while moving the fiber from C₁₀ to C₅. The reconstructed video (provided as a suppl. material) shows good reconstruction quality for the GMVAE. As seen in the reconstructed video, it is expected that the GMVAE fails to reconstruct images when objects leave the field-of-view

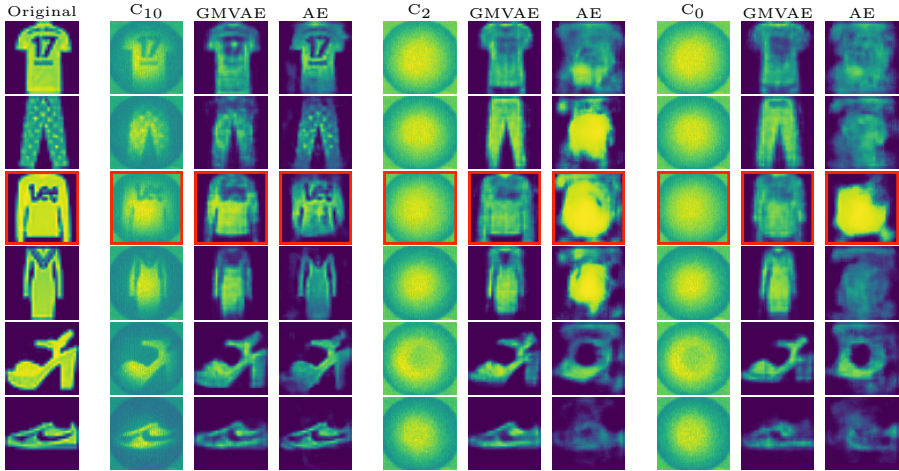


Fig. 6: First experiment with wavefront shaping: reconstruction results at the following configurations: C_{10} , C_2 and C_0 . The first column represents the original images and each 3 consecutive columns show the APD measurements, GMVAE reconstruction and AE reconstruction. Images highlighted with red squares correspond to new classes which were not used during training and the intensity of all images is in the range $[0, 1]$.

(FOV) of the fiber. We believe this could be improved using more complex VAE architectures allowing translation-blind classification [44–46].

6 Conclusion

MMFs are very attractive in imaging applications owing to their high resolution and compact dimensions. However, fiber bending is still a major challenge for leveraging MMFs in flexible imaging systems. Current MMF imaging methods either require a calibration step every time the fiber is bent or require access to the distal end of the fiber which is impractical for real-time imaging applications. In this paper, we have proposed an imaging system leveraging MMFs which requires no access or feedback signal from the distal end of the fiber. The system utilizes two MMFs placed along each other; the first MMF illuminates the object of interest with random speckle patterns and the second captures the back-scattered signal to be recorded by an APD placed at the proximal side. Objects from different classes are efficiently classified and reconstructed from the APD measurements leveraging a Gaussian mixture variational autoencoder (GMVAE). The essence of GMVAE is to learn a low-dimensional representation from measurements corresponding to different configurations of the fiber. The learnt representation is configuration-agnostic, i.e. only features of the measurements related to the underlying objects are preserved in the latent space and configuration-dependent features are discarded. This allows for imaging at new fiber configurations. The demonstrated results

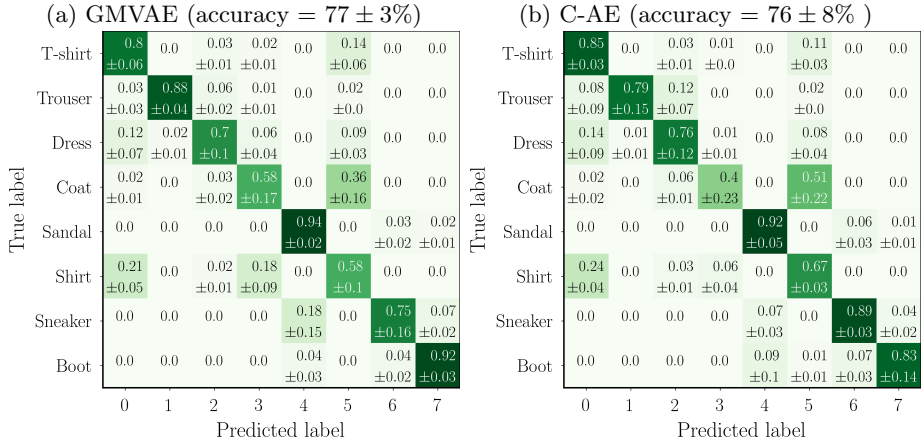


Fig. 7: First experiment with wavefront shaping: average confusion matrices obtained by (a) GMVAE and (b) C-AE on 8000 numerical measurements from the 8 trained-on classes. The confusion matrices are averaged over the unseen configurations (C_9 , C_8 , C_6 , C_4 , C_2 and C_0).

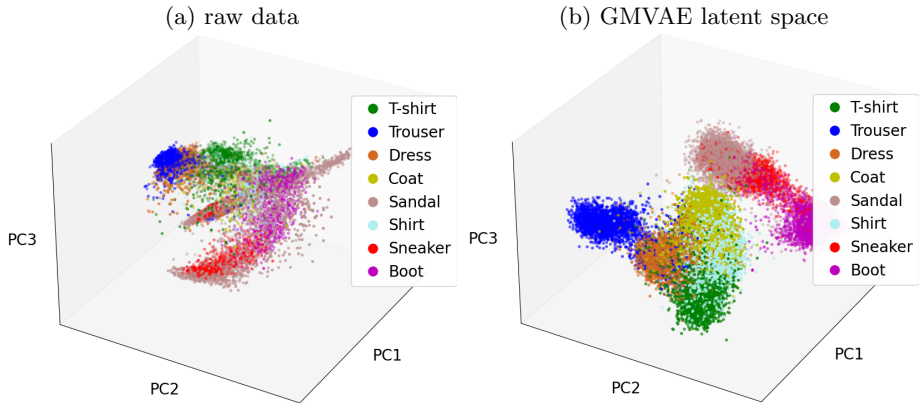


Fig. 8: First experiment with wavefront shaping: (a) combined raw data and (b) combined GMVAE latent vectors of 8000 numerical measurements computed at the configurations: C_{10} , C_2 and C_0 and projected by PCA to the 3D space.

proved the efficiency of the proposed approach in reconstruction and classification of images for new configurations of the fiber. This approach paves the way for real-time, flexible and high resolution imaging system for use in areas with very limited access.

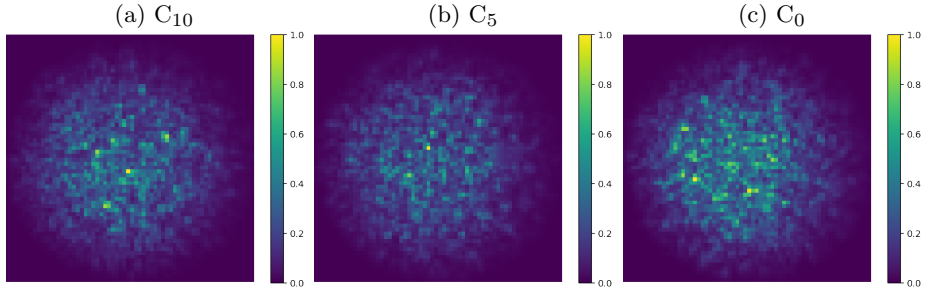


Fig. 9: Second experiment without wavefront shaping: speckles from a fixed DMD phase mask recorded at different fiber configurations: (a) C_{10} , (b) C_5 and (c) C_0 .

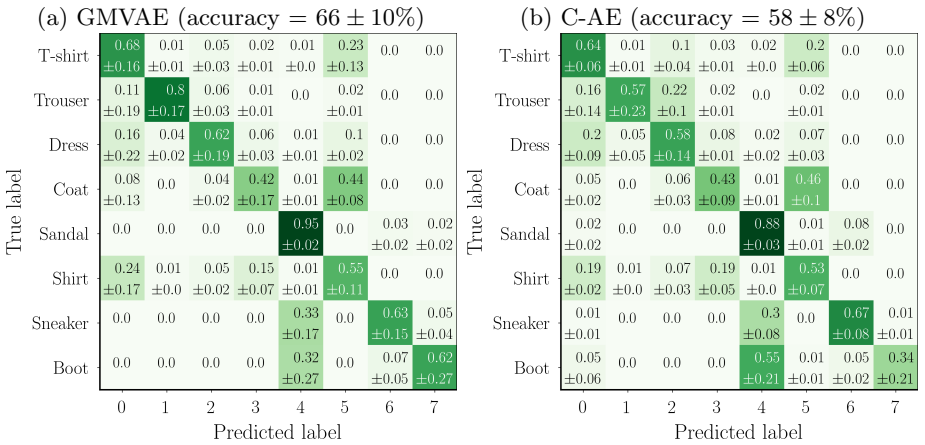


Fig. 10: Second experiment without wavefront shaping: average confusion matrices obtained by (a) GMVAE and (b) C-AE on 8000 numerical measurements from the 8 trained-on classes. The confusion matrices are averaged over the unseen configurations (C_9 , C_8 , C_6 , C_4 , C_2 and C_0).

7 Data availability

All data and codes will be made available on GitHub upon the publication of this work.

8 Acknowledgments

This work was supported by the Royal Academy of Engineering under the Research Fellowship scheme RF201617/16/31 and by the Engineering and Physical Sciences Research Council (EPSRC) Grant number EP/T00097X/1.

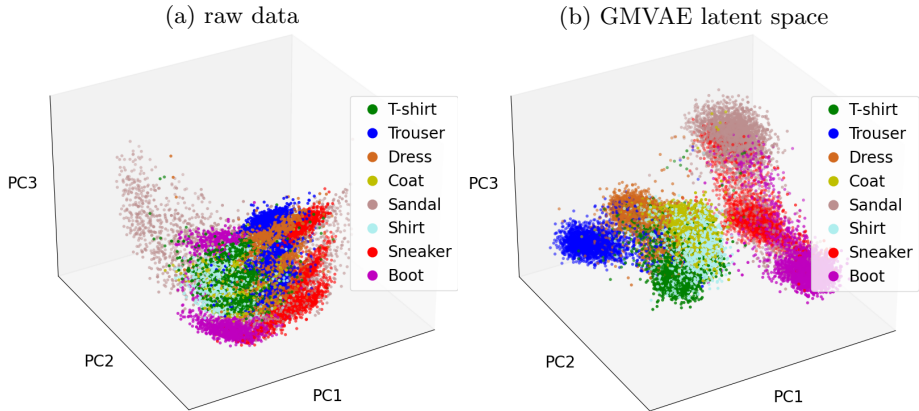


Fig. 11: Second experiment without wavefront shaping: (a) combined raw data and (b) combined GMVAE latent vectors of 8000 numerical measurements computed at the configurations: C_5 , C_2 and C_0 and projected by PCA to the 3D space.

References

- [1] Psaltis, D., Moser, C.: Imaging with multimode fibers. *Optics and Photonics News* **27**(1), 24–31 (2016)
- [2] Stellinga, D., Phillips, D.B., Mekhail, S.P., Selyem, A., Turtaev, S., Čižmár, T., Padgett, M.J.: Time-of-flight 3d imaging through multimode optical fibers. *Science* **374**(6573), 1395–1399 (2021)
- [3] Choi, Y., Yoon, C., Kim, M., Yang, T.D., Fang-Yen, C., Dasari, R.R., Lee, K.J., Choi, W.: Scanner-free and wide-field endoscopic imaging by using a single multimode optical fiber. *Physical review letters* **109**(20), 203901 (2012)
- [4] Čižmár, T., Dholakia, K.: Exploiting multimode waveguides for pure fibre-based imaging. *Nature communications* **3**(1), 1–9 (2012)
- [5] Bianchi, S., Di Leonardo, R.: A multi-mode fiber probe for holographic micromanipulation and microscopy. *Lab on a Chip* **12**(3), 635–639 (2012)
- [6] Plöschner, M., Tyc, T., Čižmár, T.: Seeing through chaos in multimode fibres. *Nature Photonics* **9**(8), 529–535 (2015)
- [7] Loterie, D., Farahi, S., Papadopoulos, I., Goy, A., Psaltis, D., Moser, C.: Digital confocal microscopy through a multimode fiber. *Optics express* **23**(18), 23845–23858 (2015)
- [8] Caravaca-Aguirre, A.M., Piestun, R.: Single multimode fiber endoscope.

Optics express **25**(3), 1656–1665 (2017)

- [9] Popoff, S.M., Lerosey, G., Carminati, R., Fink, M., Boccarda, A.C., Gigan, S.: Measuring the transmission matrix in optics: an approach to the study and control of light propagation in disordered media. *Physical review letters* **104**(10), 100601 (2010)
- [10] Čižmár, T., Dholakia, K.: Shaping the light transmission through a multimode optical fibre: complex transformation analysis and applications in biophotonics. *Optics express* **19**(20), 18871–18884 (2011)
- [11] Carpenter, J., Eggleton, B.J., Schröder, J.: 110x110 optical mode transfer matrix inversion. *Optics express* **22**(1), 96–101 (2014)
- [12] N’Gom, M., Norris, T.B., Michielssen, E., Nadakuditi, R.R.: Mode control in a multimode fiber through acquiring its transmission matrix from a reference-less optical system. *Optics letters* **43**(3), 419–422 (2018)
- [13] Li, S., Saunders, C., Lum, D.J., Murray-Bruce, J., Goyal, V.K., Čižmár, T., Phillips, D.B.: Compressively sampling the optical transmission matrix of a multimode fibre. *Light: Science & Applications* **10**(1), 1–15 (2021)
- [14] Amitonova, L.V., De Boer, J.F.: Compressive imaging through a multimode fiber. *Optics letters* **43**(21), 5427–5430 (2018)
- [15] Caravaca-Aguirre, A.M., Singh, S., Labouesse, S., Baratta, M.V., Piestun, R., Bossy, E.: Hybrid photoacoustic-fluorescence microendoscopy through a multimode fiber using speckle illumination. *Apl Photonics* **4**(9), 096103 (2019)
- [16] Lan, M., Guan, D., Gao, L., Li, J., Yu, S., Wu, G.: Robust compressive multimode fiber imaging against bending with enhanced depth of field. *Optics Express* **27**(9), 12957–12962 (2019)
- [17] Lan, M., Xiang, Y., Li, J., Gao, L., Liu, Y., Wang, Z., Yu, S., Wu, G., Ma, J.: Averaging speckle patterns to improve the robustness of compressive multimode fiber imaging against fiber bend. *Optics Express* **28**(9), 13662–13669 (2020)
- [18] Caravaca-Aguirre, A.M., Niv, E., Conkey, D.B., Piestun, R.: Real-time resilient focusing through a bending multimode fiber. *Optics express* **21**(10), 12881–12887 (2013)
- [19] Farahi, S., Ziegler, D., Papadopoulos, I.N., Psaltis, D., Moser, C.: Dynamic bending compensation while focusing through a multimode fiber. *Optics express* **21**(19), 22504–22514 (2013)

- [20] Gu, R.Y., Mahalati, R.N., Kahn, J.M.: Design of flexible multi-mode fiber endoscope. *Optics express* **23**(21), 26905–26918 (2015)
- [21] Li, S., Horsley, S.A., Tyc, T., Čižmár, T., Phillips, D.B.: Memory effect assisted imaging through multimode optical fibres. *Nature Communications* **12**(1), 1–13 (2021)
- [22] Moran, O., Caramazza, P., Faccio, D., Murray-Smith, R.: Deep, complex, invertible networks for inversion of transmission effects in multimode optical fibres. *Advances in Neural Information Processing Systems* **31** (2018)
- [23] Borhani, N., Kakkava, E., Moser, C., Psaltis, D.: Learning to see through multimode fibers. *Optica* **5**(8), 960–966 (2018)
- [24] Rahmani, B., Loterie, D., Konstantinou, G., Psaltis, D., Moser, C.: Multimode optical fiber transmission with a deep learning network. *Light: Science & Applications* **7**(1), 1–11 (2018)
- [25] Turpin, A., Vishniakou, I., d Seelig, J.: Light scattering control in transmission and reflection with neural networks. *Optics express* **26**(23), 30911–30929 (2018)
- [26] Kakkava, E., Rahmani, B., Borhani, N., Teğin, U., Loterie, D., Konstantinou, G., Moser, C., Psaltis, D.: Imaging through multimode fibers using deep learning: The effects of intensity versus holographic recording of the speckle pattern. *Optical Fiber Technology* **52**, 101985 (2019)
- [27] Caramazza, P., Moran, O., Murray-Smith, R., Faccio, D.: Transmission of natural scene images through a multimode fibre. *Nature communications* **10**(1), 1–6 (2019)
- [28] Fan, P., Zhao, T., Su, L.: Deep learning the high variability and randomness inside multimode fibers. *Optics express* **27**(15), 20241–20258 (2019)
- [29] Li, Y., Yu, Z., Chen, Y., He, T., Zhang, J., Zhao, R., Xu, K.: Image reconstruction using pre-trained autoencoder on multimode fiber imaging system. *IEEE Photonics Technology Letters* **32**(13), 779–782 (2020)
- [30] Zhao, J., Ji, X., Zhang, M., Wang, X., Chen, Z., Zhang, Y., Pu, J.: High-fidelity imaging through multimode fibers via deep learning. *Journal of Physics: Photonics* **3**(1), 015003 (2021)
- [31] Liu, Z., Wang, L., Meng, Y., He, T., He, S., Yang, Y., Wang, L., Tian, J., Li, D., Yan, P., *et al.*: All-fiber high-speed image detection enabled by deep learning. *Nature communications* **13**(1), 1–8 (2022)

- [32] Mitton, J., Mekhail, S.P., Padgett, M., Faccio, D., Aversa, M., Murray-Smith, R.: Bessel equivariant networks for inversion of transmission effects in multi-mode optical fibres. arXiv preprint arXiv:2207.12849 (2022)
- [33] Li, Y., Xue, Y., Tian, L.: Deep speckle correlation: a deep learning approach toward scalable imaging through scattering media. *Optica* **5**(10), 1181–1190 (2018)
- [34] Li, Y., Cheng, S., Xue, Y., Tian, L.: Displacement-agnostic coherent imaging through scatter with an interpretable deep neural network. *Optics Express* **29**(2), 2244–2257 (2021)
- [35] Starshynov, I., Turpin, A., Binner, P., Faccio, D.: Statistical dependencies beyond linear correlations in light scattered by disordered media. *Physical Review Research* **4**(2), 022033 (2022)
- [36] Resisi, S., Popoff, S.M., Bromberg, Y.: Image transmission through a dynamically perturbed multimode fiber by deep learning. *Laser & Photonics Reviews* **15**(10), 2000553 (2021)
- [37] Kingma, D.P., Welling, M.: Auto-encoding variational bayes. In: ICLR (2014)
- [38] Kingma, D.P., Welling, M.: An introduction to variational autoencoders. *Foundations and Trends® in Machine Learning* **12**(4), 307–392 (2019)
- [39] Shu, R.: Gaussian Mixture Vae: Lessons in Variational Inference, Generative Models, and Deep Nets. <http://ruishu.io/2016/12/25/gmvae/>
- [40] Figuerola, J.A.: Semi-supervised learning using deep generative models and auxiliary tasks. In: NeurIPS (2019)
- [41] Collier, M., Urdiales, H.: Scalable deep unsupervised clustering with concrete gmvae. arXiv preprint arXiv:1909.08994 (2019)
- [42] Charakorn, R., Thawornwattana, Y., Itthipuripat, S., Pawlowski, N., Manoonpong, P., Dilokthanakul, N.: An explicit local and global representation disentanglement framework with applications in deep clustering and unsupervised object detection. arXiv preprint arXiv:2001.08957 (2020)
- [43] Varolgiñes, Y.B., Bereau, T., Rudzinski, J.F.: Interpretable embeddings from molecular simulations using gaussian mixture variational autoencoders. *Machine Learning: Science and Technology* **1**(1), 015012 (2020)
- [44] Franceschi, J.-Y., Delasalles, E., Chen, M., Lamprier, S., Gallinari, P.:

- Stochastic latent residual video prediction. In: International Conference on Machine Learning, pp. 3233–3246 (2020). PMLR
- [45] Wu, B., Nair, S., Martin-Martin, R., Fei-Fei, L., Finn, C.: Greedy hierarchical variational autoencoders for large-scale video prediction. In: Proceedings of the IEEE/CVF Conference on Computer Vision and Pattern Recognition, pp. 2318–2328 (2021)
- [46] Wang, L., Tan, H., Zhou, F., Zuo, W., Sun, P.: Unsupervised anomaly video detection via a double-flow convlstm variational autoencoder. *IEEE Access* **10**, 44278–44289 (2022)